Turkish Journal of Electrical Engineering & Computer Sciences

http://journals.tubitak.gov.tr/elektrik/

Research Article

Turk J Elec Eng & Comp Sci
(2019) 27: 4361 – 4377

doi:10.3906/elk-1903-7

Automatic prostate segmentation using multiobjective active appearance model in MR images

Ahad SALIMI[1], **Mohamad Ali POURMINA**[1*], **Mohammad-Shahram MOIN**[2]
[1]Department of Electrical and Computer Engineering, Science and Research Branch, Islamic Azad University, Tehran, Iran
[2]Faculty of Information Technology, ICT Research Institute, Tehran, Iran

Received: 01.03.2019 • **Accepted/Published Online:** 01.07.2019 • **Final Version:** 26.11.2019

Abstract: Prostate cancer is the second largest cause of mortality among men. Prostate segmentation, i.e. the precise determination of the prostate region in magnetic resonance imaging (MRI), is generally used for prostate volume measurement, which can be used as a potential prostate cancer indicator. This paper presents a new fully automatic statistical model called the multiobjective active appearance model (MOAAM) for prostate segmentation in MR images. First, in the training stage, the appearance model, including the shape and texture model, is developed by applying principal component analysis to the training images, already outlined by a physician. Then noise and roughness are properly removed in the preprocessing step by Sticks filter and nonlinear filtering. This helps us provide the proper conditions for the prostate region detection. Finally, in order to detect the prostate region, a new multiobjective function is optimized using a suitable search algorithm. The proposed method has been applied to prostate images for segmenting the prostate boundaries. The evaluation results indicate that the presented method can yield a DSC value of $87.4 \pm 5.00\%$, is less sensitive to the edge information and initialization, and has a stronger capture range in comparison with existing methods.

Key words: Active shape model, active appearance model, prostate segmentation, genetic algorithm, objective function, nonlinear filtering

1. Introduction

Prostate cancer is the most important recognized cancerous disease (164690 of 856370) and is the second cause of mortality (after lung cancer) among American men (29430 of 323630) [1]. There are different methods to distinguish and cure prostate cancer, such as the prostate-specific antigen (PSA) test, prostatectomy (PR), and high-intensity focused ultrasonography (HIFU). Magnetic resonance imaging (MRI) is also used as a powerful technique in different treatment cases such as measuring the prostate volume, applying tumor biopsy, and determining disease development [2]. In many treatment and diagnosis methods (i.e. prostate volume measurement), the prostate area is often outlined by a physician. On the other hand, outlining the prostate boundaries is a time-consuming and tedious process, which inevitably leads to more human mistakes. Therefore, designing an automatic prostate segmentation system for MR images can be helpful. Nevertheless, low contrast conditions, presence of noise, weak edges, and similarity of the adjacent textures make prostate image segmentation complicated and challenging. The existing methods for prostate segmentation can usually be categorized into

*Correspondence: pourmina@srbiau.ac.ir

four major categories: contour and shape-based methods, region-based methods, supervised and unsupervised clustering-based methods, and hybrid methods [3].

Contour and shape-based methods employ some features such as line and edge information to detect the prostate area. However, the final results may not be accurate due to the unreliability of the line and edge information. Note that some researchers have combined an active appearance model (AAM) and multiple level-sets to automatically identify the peripheral zone (PZ) and central gland (CG) regions of the prostate area [4]. The proposed method does not depend on the landmark point problems in comparison with the traditional AAM. The same authors also worked on prostate MRI segmentation using the level-sets scheme to overcome the issues related to the landmarks' determination [5]. It determines the desired object in the new image by applying a registration-based method. Other prostate region segmentation works include a level-set based model that uses shape and texture data to predict the model and positional parameters [6] and a 3-D scheme based on matched shape contents with AAM, which utilizes PCA to combine the shape information [7]. Chandra et al. [8] proposed an automatic deformable model for prostate segmentation in MR images. They created a deformable model by applying the case-specific processing to a new scan. Finally, the created model iteratively regulates a surface to match the prostate edges. A multistart optimization framework and a minimum description length group-wise image registration scheme were utilized to automatically locate the AAM model in MR images [9]. In the method presented by Ling et al. [10], they combined a patient-specific learning method and a population learning method to segment the prostate region in 3-D CT images. They trained the mentioned models and calculated their similarities to detect the prostate pixels. Finally, an adaptive threshold method extracted the prostate region.

In region-based methods, the local intensity information and some statistical features including standard deviation, mean, and covariance are usually used in an optimization framework for prostate region segmentation. In these methods, the accuracy of the obtained results generally depends on the energy function definition and performance of the optimization algorithm. Egger et al. [11] extracted a 3-D shape of the prostate by rendering the results yielded by a semiautomatic 3-D graph-cut. They extracted the central point of the prostate region using the proposed method in [12]. Tian et al. [13] optimized a combined cost function using a graph-cut to detect the prostate area. The cost function was also formed based on two super pixel-based smoothness terms, a super pixel-based shape data term, and an appearance data term. Other papers presented several techniques including a graph-cut-based algorithm that uses semantic data resulting from random forest clustering to construct an energy function [14], a mapping transform framework that creates an adjusted edge distance map to detect the prostate boundaries [15], a new multi-atlases sparse fusion that uses the subclass discriminate analysis to estimate the prostate voxels [16], and an automatic adapted atlas-based method (CUMED) [17].

Clustering-based methods use image features including intensity and frequency response of filters to classify images. Khurd et al. [18] suggested a supervised clustering-based plan, which used the Gaussian mixture model to classify the CG area. Other researchers utilized a trained, supervised plan based on random forest clustering, employing the statistical data of shape and appearance (CAMP TUM2) [19]. Convolutional neural networks (CNN) have been widely utilized to detect prostate area in MR images in the last few years. As an example, the authors in [20] used the CNN algorithm to segment the prostate edges at the midgland slice of TRUS images. They utilized the results obtained at the midgland slices to deform a statistical shape model to detect the prostate region in the other slices. Yu et al. [21] introduced a 3-D CNN, which increased the obtained results' accuracy using backpropagation of the gradient flow and forward propagation of the location

data. Other papers have also reported a combination of CNN either with an optimizing manner [22] or a model created by an adaptive feature boosting method [23]. A new random walk algorithm-based method was presented by Ling et al. [24]. To perform automatic prostate segmentation of the image slices (except for the midgland slice), the authors combined the classification and context information to define the patient-specific and applicable population knowledge.

Hybrid schemes utilize some combination features such as shape information, region texture, and data creation by clusters for better performance in the presence of image artifacts and noise. Martin et al. [25] proposed a combination of graph-cut and level-sets method in an iterative hybrid system for a 3-D object estimation in MR images. Although the level-sets-based algorithms are more accurate than similar algorithms in other works, they have a high computational cost. Accordingly, the authors employed a 3-D graph-cut to initialize the level-set method. Another group employed a combination of fully convolutional networks (FCNs) and fully convolutional residual networks (FC-ResNets) to generate segmentation prediction using the normalized images refined via FC-ResNet [26].

This paper proposes a novel and appropriate system based on the statistical shape and appearance model for prostate segmentation in MR images. We define a new objective function using the edge, texture, position, and shape information to efficiently overcome the AAM's problems. Noise sensitivity, finite capture range, low flexibility of the model contour, and the need for initial placement are typical problems of the AAM that is widely utilized in medical object segmentation. The position function has been considered to improve the capture range. The image roughness and extra edge are smoothed in a preprocessing step and the noise sensitivity decreases using both texture and edge information in the search step. To obtain accurate segmentation, in the search stage, the model's shape is compared with a reference shape, and then the shape of the model is changed based on the comparison results. This helps us to make our system a feedback system.

The remainder of this paper is organized as follows: Section 2 presents the prostate boundaries detection stages, including the background of the model reconstruction, preprocessing, energy function, and search algorithm. Section 3 describes the detailed experiments, datasets and results. Section 4 gives a brief discussion, and Section 5 concludes the paper.

2. Proposed automatic prostate segmentation system

Figure 1 represents the block diagram of the proposed method. The training step involves developing the AAM model, including the shape and texture model. In this step, PCA is applied to the information extracted from training images to create the AAM. In the segmentation phase, first, the images corrupted with noise and roughness are filtered in the preprocessing step. Then the prostate area is segmented using a proper optimization framework. In this section, each of the mentioned steps is described in detail.

2.1. Background and model reconstruction

As seen in Figure 2, the AAM is created by combining the shape and texture models. Here, the shape and texture models are generated using the analysis presented in [27]. First, a physician manually outlined the prostate area in each image of the training images. Accordingly, the shape vector of each image can be defined as follows:

$$\begin{aligned} \overline{X_i} &= [x_{i0}, y_{i0}; x_{i1}, y_{i1}; ....x_{in}, y_{in}]^T, \\ \overline{X} &= [\overline{X_1}, \overline{X_2}....\overline{X_i}], \end{aligned} \tag{1}$$

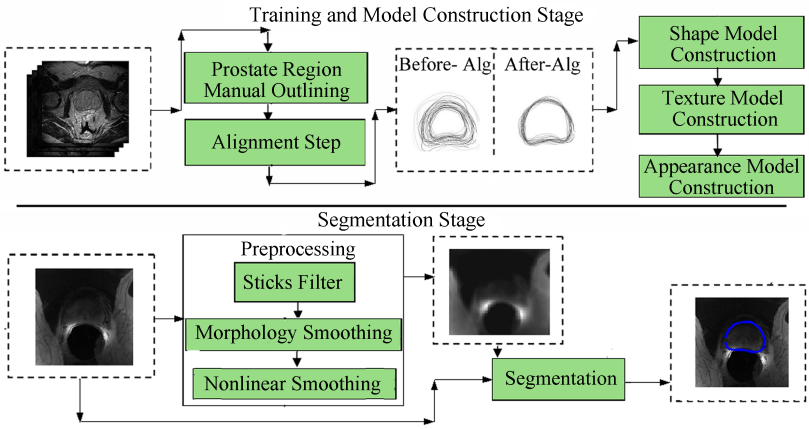

Figure 1. The block diagram of the proposed system. The proposed system consists of two main stages. First, the model is created. In the segmentation phase, after a proper preprocessing step, the prostate boundaries are extracted by a new optimization method.

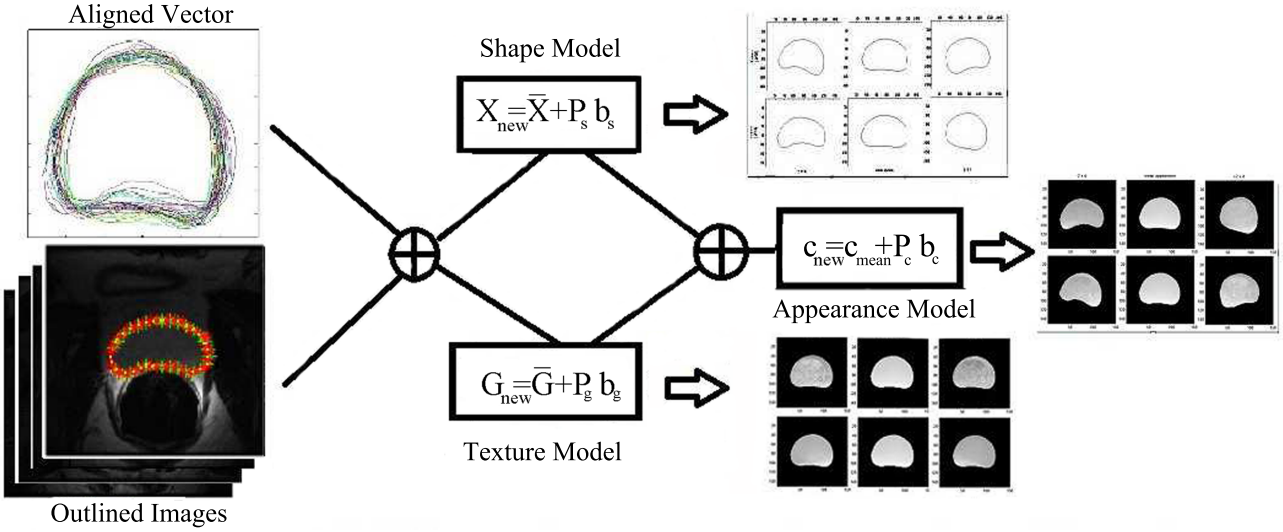

Figure 2. The active appearance model construction steps. First, the manually outlined shape vectors are aligned. Then the shape and texture model are created using two separate PCA steps. Finally, two models are combined and the appearance model is constructed.

where $\overline{X_i}$ is the shape vector of the ith image, $[x_{in}, y_{in}]$ is the coordinate of the nth landmark point, and i and n represent the numbers of the training images and landmark points, respectively. The shape vectors are aligned using the Procrustes method and then PCA is applied to the aligned shape vectors ($\overline{X_i}$). Finally, the shape model is given by (2):

$$\overline{X_{New}} = \overline{\overline{X}} + \overline{P_s b_s}, \overline{\overline{X}} = \frac{1}{i}\sum_{k=1}^{i} \overline{X_k}, \tag{2}$$

where $\overline{\overline{X}}$ is the mean shape, $\overline{P_s}$ contains the eigenvectors of the covariance matrix (which are the principal components of the shape model), and $\overline{b_s}$ is the shape model parameter, which controls the model deformation.

A similar analysis is applied to generate the texture model. Here, before the PCA implementation, the intensities of the prostate area should be formed as a texture vector. As shown in Figure 3, first, the prostate

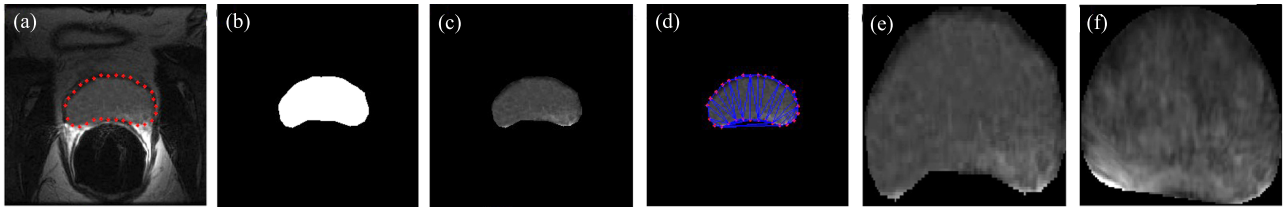

Figure 3. The texture model construction steps: (a) area outlined by physician and landmark points, (b) mask image, (c) extracted prostate area using the mask image, (d) patched prostate area using the landmark points, (e) image before wrapping step, and (f) image after wrapping step.

area (which was outlined by the physician) is masked in each image (see Figures 3a–3c). Then the mask image is patched according to the landmark points (Figure 3d). Next, the resulting patches are wrapped to the mean shape using the method presented in [28] (Figures 3e and 3f). Finally, the intensities of the prostate area in the wrapped image are converted to the texture vector. Hence, the texture vectors can be defined as follows:

$$\overline{G} = [\overline{g_1}, \overline{g_2}, ...\overline{g_i}], \tag{3}$$

where $\overline{g_i}$ is the texture vector of the ith image and i is the number of training images. PCA is performed on the texture vectors ($\overline{G}$), after which the texture model is calculated using (4):

$$\overline{G_{New}} = \overline{\overline{G}} + \overline{P_g b_g}, \overline{\overline{G}} = \frac{1}{i}\sum_{k=1}^{i} \overline{g_k}, \tag{4}$$

where $\overline{\overline{G}}$ is the mean texture vector, $\overline{P_g}$ includes eigenvectors of the covariance matrix, and $\overline{b_g}$ represents the texture model parameter, which controls the intensity changes in the texture model.

As mentioned earlier, the shape and the texture model are controlled by $\overline{b_s}$ and $\overline{b_g}$. In order to create the AAM, these parameters have been combined using (2) and (4), as follows:

$$\overline{c} = \begin{bmatrix} \overline{W_s b_s} \\ \overline{b_g} \end{bmatrix}, \overline{c} = \begin{bmatrix} \overline{W_s P_s}^T (\overline{X} - \overline{\overline{X}}) \\ \overline{P_g}^T (\overline{G} - \overline{\overline{G}}) \end{bmatrix}, \tag{5}$$

where $\overline{c}$ is the appearance vector and $\overline{W_s}$ represents a diagonal matrix revealing the weights of the shape model parameters. The appearance vectors are calculated using (5) for each of the training images ($\overline{C} = [\overline{c_1}, \overline{c_2}, \overline{c_3}, ...\overline{c_i}]$). Then PCA is applied to the appearance vectors, and finally the AAM is found by (6):

$$\overline{C_{New}} = \overline{C_{mean}} + \overline{P_c b_c}\,|_{\overline{C_{mean}} \simeq 0} \simeq \overline{P_c b_c}, \overline{C_{mean}} = \frac{1}{i}\sum_{k=1}^{i} \overline{c_k} \simeq 0, \tag{6}$$

where $\overline{P_c}$ includes eigenvectors of the covariance matrix (which are the principal components of the AAM), and $\overline{b_c}$ denotes the appearance model parameter, which controls both the intensity changes and the shape deformation of the AAM. The shape deformation and the texture changes of the AAM can be directly obtained as follows:

$$\begin{matrix} \overline{X_{New}} = \overline{\overline{X}} + \overline{P_s W_s}^{-1} \overline{P_{cs} b_c} \\ \overline{G_{New}} = \overline{\overline{G}} + \overline{P_g P_{cg} b_c} \end{matrix}, \overline{P_c} = \begin{bmatrix} \overline{P_{cs}} \\ \overline{P_{cg}} \end{bmatrix}, \tag{7}$$

where the lengths of $\overline{P_{cs}}$ and $\overline{P_{cg}}$ are equal to the lengths of $\overline{X_i}$ and $\overline{g_i}$, respectively.

2.2. Preprocessing

The MR images utilized in this work were highly corrupted by noise and roughness, which could lead to local extreme points. On the other hand, the weak edges in these types of images make the conventional methods such as Gaussian and low-pass filters not suitable for the noise removal. Therefore, to address the mentioned problem, a preprocessing stage including the Sticks filter [29], morphology smoothing, and anisotropic diffusion filter has been considered before the segmentation step. In the first step of preprocessing, Sticks filters are applied for eliminating the noise to improve the contrast of the MR images. In the next stage, morphological smoothing including top-hat and bottom-hat transform is used to remove the undesirable effects of the Sticks filter, as shown in (8):

$$\overline{SI} = \overline{SFI} + \overline{THI} - \overline{BHI}, \tag{8}$$

where $\overline{SI}$ and $\overline{SFI}$ are the smoothed image and the results obtained by the Sticks filter, respectively. $\overline{THI}$ and $\overline{BHI}$ represent top-hat and bottom-hat transform of the Sticks filter output, which are obtained by (9):

$$\overline{THI} = \overline{SFI} - (\overline{SFI} \circ \overline{B_m}), \overline{BHI} = \overline{SFI} - (\overline{SFI} \bullet \overline{B_m}), \tag{9}$$

where $\overline{B_m}$ is a structuring element and $\circ$ and $\bullet$ are the opening and closing operands, respectively. Lastly, a nonlinear method, the anisotropic diffusion filter (ADF), is used to reduce the effect of filtering in the proximity of edges. The ADF was thoroughly studied in [30].

2.3. Objective function

We have proposed a novel objective function to segment the prostate area in new images. Suppose the position of the AAM in the new image is defined as follows:

$$\overline{X_{New}} = F(\overline{\overline{X}} + \overline{P_s b_s}, t, s, \theta), \tag{10}$$

where t, s, θ, and b_s are translation, scaling, rotation, and deformation parameters, respectively. On the other hand, the objective function should be defined as in an optimizing problem to find the best position of the AAM. Accordingly, it can be generally defined as (11):

$$\overline{Y} - F(\overline{X_{model}}, t, s, \theta) = 0, \tag{11}$$

where $\overline{Y}$ is the best position (prostate area) for $\overline{X}$. Since in (11), $\overline{Y}$ is the prostate area boundaries, and on the other hand, there is enough information about the exact position of the prostate area, in this work, the prostate region features have been used instead of $\overline{Y}$. Accordingly, the objective function is defined as follows:

$$E = \left[{}^{1}/_{(E_{pos})} \right] \times \left[\alpha E_{edge} + \beta E_g + \gamma E_{Shape} \right], \tag{12}$$

where α, β, and γ determine the effects of each energy function. In (12), E_{edge}, E_g, E_{pos}, and E_{Shape} represent the edge energy, the texture energy, the position energy, and the shape energy, respectively. The proposed objective function should be minimized to detect the prostate boundaries.

The position energy (E_{pos}) increases the capture range of the proposed method in comparison with previous works. It shows the correct position probability of the shape model in the searching step whose value

is 0–1. A value equal to 0 means that the model is far from the prostate area while a value close to 1 suggests that the model is near the prostate area. Therefore, the shape model is automatically attracted to the prostate area using the position energy. The value of the position energy is calculated as follows:

$$\overline{E_{pos}} = \left({}^{1}/_{A_m}\right) \sum_{k_1=1}^{x} \sum_{k_2=1}^{y} e_{pos}(k_1, k_2), \tag{13}$$

where A_m is the area of the model mask and e_{pos} is obtained by (14):

$$e_{pos}(x, y) = p(x, y) \bullet \overline{BW_{model}}(x, y), \tag{14}$$

where $\bullet$ and $\overline{BW_{model}}$ are the AND operand and the model mask (a binary image – the inside and outside of the model area are selected as 0 and 1), respectively, and $p(x, y)$ denotes the position possibility, which is defined as follows:

$$p(x, y) = \left({}^{1}/_{i}\right) \sum_{k=1}^{i} \overline{BW_k}(x, y), \tag{15}$$

where $\overline{BW_k}$ are the mask images (in a binary image, the inside and outside of the prostate area, which are outlined in the training step by a physician, have the values of 0 and 1, respectively) and i indicates the number of training images. The final value of E_{pos} can be corrected for more accurate segmentation as follows:

$$E_{pos} = \begin{cases} E_{pos} E_{pos} < th \\ 1 E_{pos} >= th, \end{cases} \tag{16}$$

where $th \geq 0.5$ is a threshold parameter (in this work, the value of 0.75 has been assigned to th based on the test's results). Figure 4 reveals the results obtained using (15) (Figure 4a) and (16) (Figure 4b).
The edge energy (E_{edge}), defined in (17), pushes the model to the object's edges in the image:

$$E_{edge} = \sum_{k=1}^{n} {}^{1}/\Delta(G * I(x_k, y_k)), \tag{17}$$

where I, $[x_k, y_k]$, G, and $*$ are the input image, model coordinates, Gaussian filter mask, and linear convolution operator, respectively. Other external energies including gradient vector flow (GVF) [31] and vector field convolution (VFC) [32] can be used as the edge energy to improve the capture range of the proposed method. However, we have not considered these energies, since they have a high computational cost.

Since there is some information of the prostate area texture in the AAM, it can produce a texture similar to the prostate area using (7). Therefore, the texture energy is defined as in (18):

$$E_g = \sqrt{\sum_{k=1}^{l} \left(\overline{g}_{model_k} - \overline{g}_{image_k}\right)^2}, \tag{18}$$

where $\overline{g}_{model}$ and $\overline{g}_{image}$ are the intensity vectors (with length of l) of the texture generated by the models and texture available in the inner area of the model contour in the image, respectively.

The shape of the model is deformed in the searching step. Therefore, the shape energy is defined to avoid unfavorable model deformation. This energy determines the extent of difference between shapes. Therefore, the

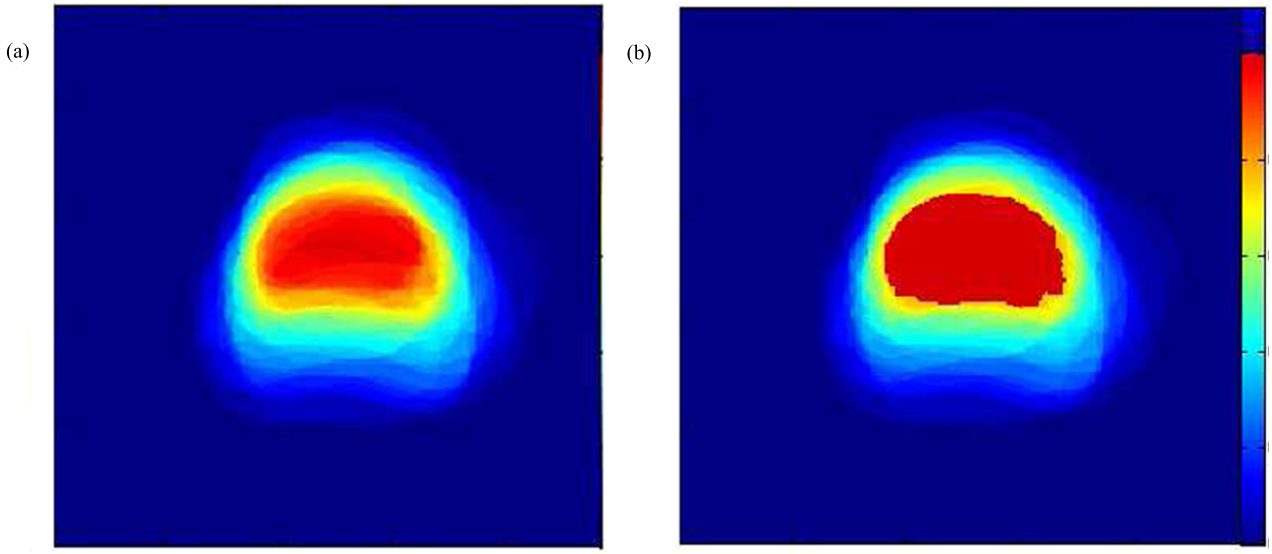

Figure 4. The position energy: (a) before thresholding and (b) after thresholding.

shape energy can control (using determination of γ) the model deformation, when its shape is compared with a reference shape (mean shape). In order to obtain the shape energy, a new index, called S_{Index}, is defined as follows:

$$S_{Index} = \frac{P}{A} \times \bar{D}, \tag{19}$$

where P is the perimeter of the shape, A represents the area of the shape, and $\bar{D}$ denotes a distance parameter, which determines the distance between the points on the shape boundary and the shape gravity center, and is defined as follows:

$$\bar{D} = \sum_{k=1}^{n} D_k, \overline{D} = [D_1, D_2, ..., D_n], D_k = \sqrt{(x_k - x_c)^2 + (y_k - y_c)^2}, \tag{20}$$

where $[x_c = \frac{1}{n}\sum_{k=1}^{n} x_k, y_c = \frac{1}{n}\sum_{k=1}^{n} y_k]$ are the coordinates of the shape gravity center. Suppose that there are two similar shapes, where the second shape is S times larger than the first shape. In this case, the distance between two shapes can be calculated as follows:

$$\begin{array}{l} A_2 = S^2 A_1 \\ P_2 = SP_1 \\ \bar{D}_2 = S\bar{D}_1 \end{array} \rightarrow S_{Index_2} = \frac{P_2}{A_2}\bar{D}_2 = \frac{SP_1}{S^2 A_1} S\bar{D}_1 = \frac{P_1}{A_1}\bar{D}_1 = S_{Index_1}. \tag{21}$$

Therefore, two similar shapes with a different scale have equal S_{Index}. According to Figure 5, the distance vector is obtained for each shape to eliminate the aligning phase (in the usual comparison methods, first, two shapes should be aligned). As shown geometrically, when the distance vector is calculated, it is tantamount to the transmission of the shape to the coordinate center. Based on the mentioned point, the shape energy can be calculated using (22):

$$E_{Shape} = \begin{cases} S_{Index_1} - S_{Index_2} & \frac{1}{L} < V < L \\ |S_{Index_1} - S_{Index_2}| & otherwise, \end{cases} \tag{22}$$

Algorithm 1 Optimizing algorithm.

Start
$E_{old} \leftarrow \infty, pos_{old} \leftarrow X_{initial}, t = t_{old} \leftarrow 0, S = s_{old} \leftarrow 0, \theta = \theta_{old} \leftarrow 0, I_t \leftarrow 0, K \leftarrow 25$ [1].
loop
  $I_t \leftarrow I_t + 1$
  $C = [x_{mc}, y_{mc}]$ [2].
  $C_{P_{max}} = [x_{P_{max}}, y_{P_{max}}]$ [3].
  $L = [d_x, d_y] = [(x_{mc} - x_{P_{max}})], (y_{mc} - y_{P_{max}})$.
  $X_{new} = S \times \begin{bmatrix} \cos\theta & -\sin\theta \\ \sin\theta & \cos\theta \end{bmatrix} \times (pos_{old}) + (t + L)$.
  $E_T = E(pos)$.
  if $E_T > E_{old}$ **then**
    $pos \leftarrow pos_{old}$
  else
    $E_{old} \leftarrow E_T, pos_{old} \leftarrow pos, t_{old} \leftarrow t, S_{old} \leftarrow S, \theta_{old} \leftarrow 0$.
  end if
  $S = S_{old} + step_s, t = told + step_t, \theta = \theta_{old} + step_\theta$.
  if $I_t > K$ **then**
    Break
  end if
end loop
End

where $L \simeq 1$, $V = \left| \frac{(\frac{P_1}{S_1} \times D_1)}{(\frac{P_2}{S_2} \times D_2)} \right|$, and Var are the variance operators. The proposed index, which calculates the similarity of two shapes, does not need any aligning phase. Therefore, the utilized S_{Index} in the shape energy can improve the speed of the search algorithm.

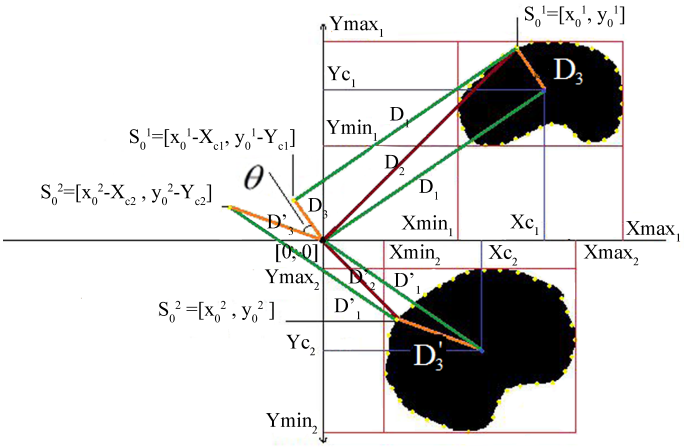

Figure 5. The S_{Index} structure: S_{Index} does not need the aligning step for comparison of two shapes.

2.4. Search algorithm

In this section, we present an appropriate algorithm to minimize the presented objective function (12). The deformation parameters, including t, s, θ, and b_s, were not directly involved in the objective function. This indicates that the objective function was not directly modeled based on the search parameters. Therefore, the classic optimization methods are not suitable in our case. Here, we employed a new search algorithm, with two main steps, to accurately segment the prostate region. The first step was finding the prostate location in the image, and the second step was determining accurate prostate boundaries. t, s, and θ play a major role in finding the prostate location and b_s has a vital role in detecting accurate prostate boundaries in the image. As

shown in Algorithm 1, an iterative method is presented to detect the prostate location. In this algorithm, b_s is considered equal to 0 where an iterative framework estimates the position of prostate area using the objective function parameters, $Step_t$, $Step_s$, and $Step_\theta$. $Step_t$, $Step_s$, and $Step_\theta$ determine the changes rate of t, s, and θ in (10). They deform the model position in the search algorithm. The search algorithm stops when the iteration number of the search algorithm is equal to K. One should obtain the shape parameter for a more accurate segmentation of the prostate boundaries. Therefore, the genetic algorithm has been used to find the shape parameter in the second step. The mentioned steps were performed in a pyramidal framework to obtain a more accurate optimization. In the pyramidal framework, the original image was considered as level-0 and the next image in level-1 was obtained by smoothing and subsampling of level-0, which was an image with half size. The next levels were achieved from the previous level, by further smoothing and subsampling.

3. Experiments and results

The proposed method was tested on T2-weighted MR images provided by the MICCAI Prostate MR Image Segmentation (PROMISE12) challenge. There were 50 and 30 images in the training and test datasets, respectively. The mentioned datasets were acquired with different clinical settings.

In the preprocessing stage, the Sticks filter was used twice and the length of its masks was considered as 5 and 15. The element structure used in the morphological smoothing step was a disk, with a length of 5, as follows:

$$\overline{B}_m = \begin{bmatrix} 0 & 0 & 1 & 0 & 0 \\ 0 & 1 & 1 & 1 & 0 \\ 1 & 1 & 1 & 1 & 1 \\ 0 & 1 & 1 & 1 & 0 \\ 0 & 0 & 1 & 0 & 0 \end{bmatrix}. \tag{23}$$

Nonlinear smoothing was applied five times, and its parameters κ and λ (the effect of these parameters on the image was thoroughly studied in [31]) were experimentally selected as 4 and 0.143, respectively. Figure 6 displays the effect of the preprocessing stage on the contrast of a typical MR image (see Figures 6a and 6b). According to Figure 6c, the noise and roughness have been almost eliminated.

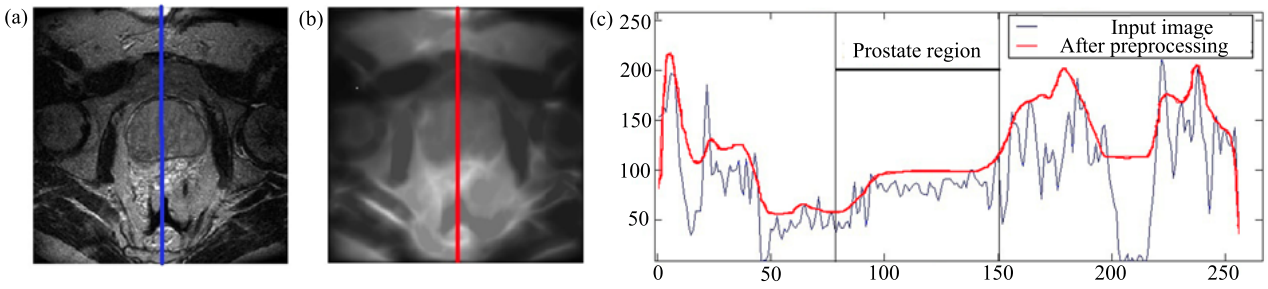

Figure 6. The effect of preprocessing stage on the image intensities: (a) image before preprocessing stage, (b) image after preprocessing stage, and (c) the middle column profile intensities of the prostate area; the prostate area has been completely smoothed and the image contrast around the prostate boundaries has been enhanced.

The algorithm presented in Section 2.4 was used to segment the prostate area in the test images. In order to achieve more accurate segmentation, the values of α, β, and γ in the objective function (12) were experimentally fixed as 1, 100, and 15, respectively. Furthermore, as illustrated in Figure 7, the average execution time for the presented method changed with elevation of K (see Figure 7a). On the other hand,

the objective function value decreased with the growth of K (see Figure 7b). Therefore, the value of K was selected as 25, to improve the algorithm execution time (see Figure 7c). The values of $step_t$, $step_s$, and $step_\theta$ were also obtained from the following vectors, respectively:

$$step_t = \begin{bmatrix} x_t \\ y_t \end{bmatrix} = \begin{cases} x_t = [0,0,0,0,0,-2,-1,1,2] \\ y_t = [-2,-1,0,1,2,0,0,0,0] \end{cases}, \quad step_s = [-.15 - .0750.075.15], step_\theta = [-.10.1]. \tag{24}$$

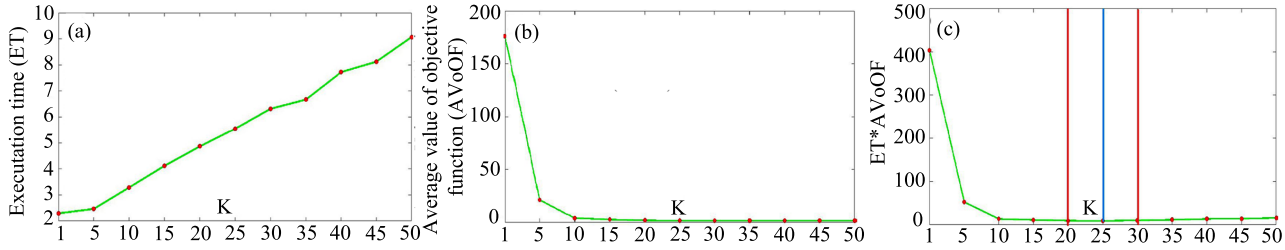

Figure 7. (a) Effect of the iteration number (K) on the execution time; (b) effect of the iteration number (K) on the segmentation accuracy; (c) the best value of K is 25 based on the test results.

The genetic algorithm was utilized to determine the shape parameter. The parameters required to perform the genetic algorithm, including the population size, the mutation rate, the fraction of the population, the number of iterations, and the number of bits in each parameter, were experimentally fixed to 100, 0.15, 0.5, 25, and 5, respectively. The pyramidal framework was done for 4 levels. Figure 8 presents the search algorithm's effect on the value of the objective function (Figure 8a) and the obtained results in a typical MR image (Figure 8b). Also, Figure 9 demonstrates the segmentation results for some typical prostate images. In some cases, the low contrast of the image reduced the segmentation accuracy, which occurred particularly in the apex slices.

4. Discussion

We have compared the accuracy of the proposed method with that of the other works presented in the MICCAI Prostate MR Image Segmentation[4] challenge. The quantitative performance of the methods presented in PROMISE12 has been evaluated using some metrics, including the Dice similarity coefficient (DSC), Hausdorff distance (HD), relative absolute volume difference (RVD), and average boundary distance (ABD). The DSC is obtained using (25):

$$DSC = 2 \times \left[{}^{(A \cap B)}/_{(A \cup B)} \right]. \tag{25}$$

The RVD is defined as follows:

$$RVD(A,B) = 100 \times \left(\frac{A}{B} - 1 \right), \tag{26}$$

where A and B are the regions segmented by the presented system and the ground truth segmentation, respectively.

[4]PROMISE12 (2012). MICCAI Prostate MR Image Segmentation [online]. Website https://promise12.grand-challenge.org [October 2012].

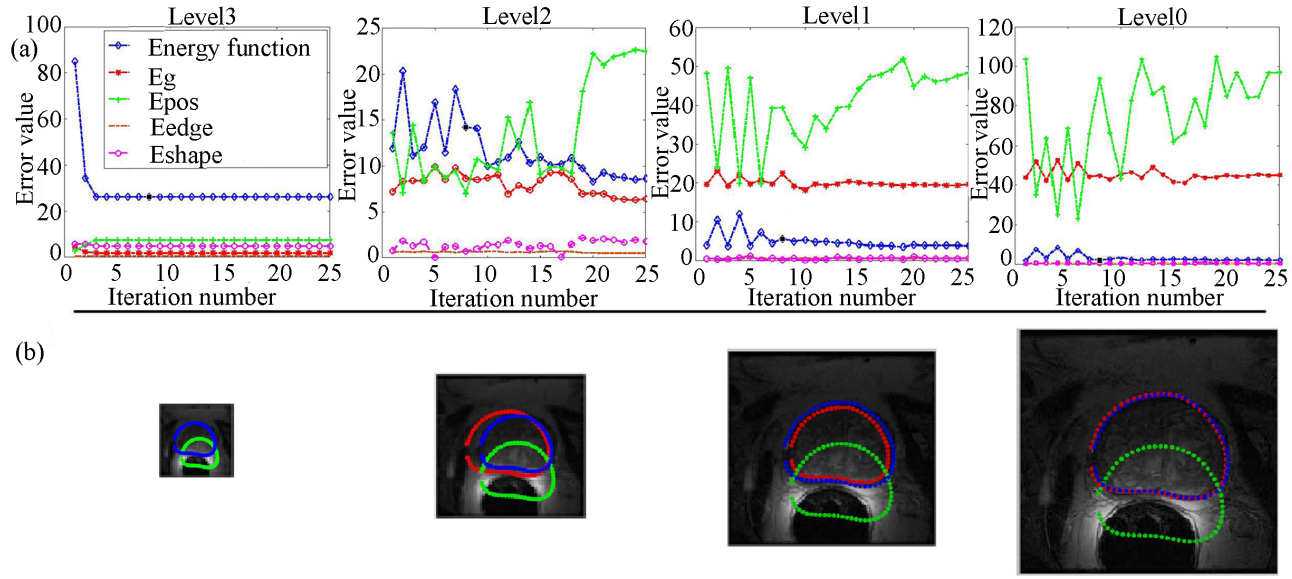

Figure 8. The segmentation pyramidal structure: (a) effect of the search algorithm on the value of the objective function at several levels; (b) the search algorithm applied in a 4-level pyramidal structure to segment the prostate area. The pyramid scheme leads to a faster and more accurate prostate area segmentation.

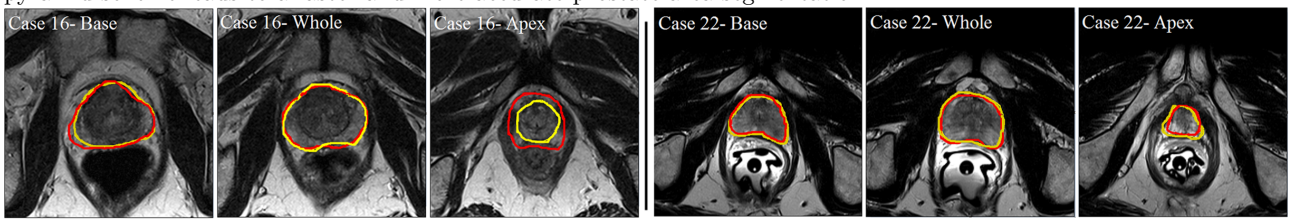

Figure 9. The segmentation results on some test images: the yellow and red contours represent the ground truth and system segmentation results, respectively. The artifacts, shadows, and tissue similarity reduced the segmentation accuracy in the apex slices. These images are available from the PROMISE12 challenge's website.

ABD is calculated using (27):

$$ABD_{(X_s,Y_s)} = \frac{\left(\sum_{x\in X_s}\min_{y\in Y_s} d(x,y) + \sum_{y\in Y_s}\min_{x\in X_s} d(x,y)\right)}{X_s + Y_s}. \tag{27}$$

Finally, regular HD distance is described as follows:

$$HD_m(X_s,Y_s) = \max_{x\in X_s}(\min_{y\in Y_s} d(x,y)), HD(X_s,Y_s) = \max(HD_m(X_s,Y_s), HD_m(Y_s,X_s)), \tag{28}$$

where X_s and Y_s are the surface points sets of the ground truth and presented system segmentation, respectively, and d is the Euclidean distance operand. The results obtained from the test phase are presented in Table 1. The average values of RVD, DSC, ABD, and HD for all of the test images have been calculated as $7.17 \pm 15.53\%$, $87.40 \pm 5.00\%$, 1.89 ± 0.44 mm, and 4.92 ± 1.43 mm, respectively. Based on the test's results, the proposed method ranked among the top 5 of the presented works. In our method, the prostate's position was estimated using the probability position function in a new image. Thus, the initial placement was not required. Meanwhile,

the segmentation results were more accurate than those of the other works in the base and middle slices, because the noise and extra edges were removed in the preprocessing step, the texture and edge information were used, and the shape of the model was always compared to a reference shape (mean shape of the prostate). As shown in Table 2, the average values of RVD, DSC, ABD, and HD for the other work by the authors (IAU) presented in [33] were obtained as 12.96%, 87.55%, 2.00 mm, and 5.32 mm in the base slices and 7.67%, 89.28%, 1.86 mm, and 5.34 mm in the middle slices, and 24.69%, 79.84%, 2.57 mm, and 6.31 mm in the apex slices, respectively. The average of the corresponding indices for our presented method (SCIRESU) were calculated as 8.18%, 88.97%, 1.81 mm, and 4.51 mm in the base slices; 6.01%, 90.20%, 1.74 mm, and 4.92 mm in the middle slices; and 7.32%, 83.30%, 2.11 mm, and 5.34 mm in the apex slices, respectively. Due to the variety of prostate shapes, the low contrast, and poor edges in MR images (especially in apex slices), the segmentation accuracy in the IAU method was somewhat lower than the presented method in this paper. In this paper, a new objective function was used that has less sensitivity to the edges than the previous one. As a result, this increased accuracy compared with previous work. Here, owing to employing PCA in the AAM creation process, the shape variation of the AAM-based method decreased. Therefore, even if the position of the prostate is correctly estimated in the apex slices, there are some cases where the precision of segmentation is reduced. As shown in Table 2, in the apex slices, the average values of RVD, DSC, ABD, and HD for the work (CUMED) were calculated and obtained as 15.18%, 86.81%, 1.74 mm, and 4.29 mm, respectively. On the other hand, the averages of the same indices for our proposed system were found as 7.32%, 83.3%, 2.11 mm, and 5.34 mm, respectively.

Table 1. Evaluation of the proposed method based on the DSC, H.D, ABD, and RVD indexes.

Metric		Whole	Base	Apex
DSC	Average	0.90±0.02	0.89±0.03	0.83±0.10
	Score	85.33±3.47	88.00±3.37	87.67±6.04
H.D	Average	4.93±1.25	4.51±1.33	5.34±1.72
	Score	86.89±3.34	89.22±3.19	87.39±4.07
ABD	Average	1.74±0.29	1.81±0.41	2.11±0.63
	Score	85.60±2.43	87.69±2.80	87.57±3.96
RVD	Average	6.01±8.45	8.18±13.66	7.33±24.50
	Score	81.20±15.44	84.80±11.34	85.60±12.86

Table 2. Quantitative comparison between the proposed method and other reported methods. According to these results, the proposed method has a better performance for the base and whole slices compared to other methods.

Name	Rank	DSC [%]			H.D [mm]			ABD [mm]			RVD [%]			Score
		Whole	Base	Apex	Whole	Base	Apex	Whole	Base	Apex	Whole	Base	Apex	
CUMED [17]	4	89.43	86.42 87.55 ± 4.00	**86.81**	5.54	5.41 5.08 ± 1.58	**4.29**	1.95	2.13 1.94 ±0.49	**1.74**	6.95	11.04 **11.06** ± **11.39**	15.18	86.65
Proposed method	5	**90.20**	**88.97** **87.4** ±**5.00**	83.30	**4.92**	**4.51** **4.92** ±**0.43**	5.34	**1.74**	**1.81** **1.89** ±**0.44**	2.11	**6.01**	**8.18** 7.17 ± 15.53	**7.32**	86.41
IAU [33]	12	89.28	87.55 86.00 ± 6.00	79.84	5.34	5.32 5.65 ± 1.81	6.31	1.86	2.00 2.14 ± 0.55	2.57	7.67	12.96 15.10 ± 14.21	24.69	84.84
Emory [11]	14	87.03	83.52 84.03 ± 5.47	81.53	5.04	6.03 5.46 ± 1.31	5.31	2.14	2.65 2.40 ± 0.56	2.41	8.64	15.70 14.89 ± 9.88	20.32	83.66
UdeM 2D [25]	16	87.42	84.93 85.5 ± 5.60	84.16	6.12	6.44 5.76 ± 2.01	4.71	2.17	2.39 2.21 ± 0.65	2.07	12.37	18.37 17.55 ± 16.58	21.90	83.02
CAMP TUM2 [19]	18	86.91	84.31 85.21 ± 3.87	84.4	5.71	5.84 5.39 ± 1.50	4.62	2.33	2.46 2.27 ± 0.61	2.03	14.98	20.84 19.01 ± 17.10	21.21	82.39
SIATMIDS [18]	22	84.29	83.2 81.08 ± 3.33	75.75	6.17	6.21 6.15 ± 2.02	6.09	2.49	2.58 2.61 ± 0.81	2.76	12.60	16.16 18.76 ± 13.40	27.51	80.85

5. Conclusions

In this paper, we have proposed a new automatic system for prostate segmentation in MR images based on the AAM. The results of simulations revealed the superiority of the proposed method in comparison with the similar reported methods. The unwanted edges and noise were efficiently removed using a proper preprocessing step, including the Sticks filter, morphology smoothing, and anisotropic diffusion filter. A preprocessing step was utilized to provide suitable conditions for more accurate segmentation. We also introduced a new objective function, which used the position, texture, edge, and shape information. Thanks to this objective function, our proposed method did not need initialization of the prostate location. In other words, the position energy was employed in the objective function to enhance the capture range of the presented model. As explained in Section 4, the segmentation accuracy also improved in comparison with that of similar works using the edge and texture information in the objective function. A new index, S_{Index}, was also introduced. This index could directly (without need of aligning the shapes) calculate the difference of the shapes. The proposed method was tested on the MICCAI Prostate MR Image Segmentation (PROMISE12) challenge, leading to a DCS accuracy of $87.4 \pm 5.00\%$. In future research, one can (1) develop a system for directly segmenting the prostate in 3-D MR images, (2) enhance the segmentation accuracy in apex slices by working on the AAM deformation method, and (3) lengthen the execution time using a better search algorithm.

References

[1] Siegel RL, Miller KD, Jemal A. Cancer statistics. CA Cancer Journal for Clinicians 2018; 68 (1): 7-30. doi: 10.3322 /caac.21442

[2] Ghose S, Oliver A, Marti R, Liado X, Vilanova JC et al. A survey of prostate segmentation methodologies in ultrasound, magnetic resonance and computed tomography images. Computer Methods and Programs in Biomedicine 2012; 108 (1): 262-287. doi: 10.3322 /caac.21442

[3] Litjens G, Toth R, Van de ven W, Hoeks C, Kerkstra S et al. Evaluation of prostate segmentation algorithms for MRI. Medical Image Analysis 2014; 18 (2): 359-373. doi: 10.3322 /caac.21442

[4] Toth R, Ribault J, Gentile J, Sperling D, Madabhushi A. Simultaneous segmentation of prostatic zones using active appearance models with multiple coupled levelsets. Computer Vision and Image Understanding 2013; 117 (1): 1051-1060. doi: 10.1016/j.cviu.2012.11.013

[5] Toth R, Madabhushi A. Multi-feature landmark-free active appearance models: application to prostate MRI segmentation. IEEE Transactions on Medical Imaging 2012; 31 (8): 1638-1650. doi: 10.1109/TMI.2012.2201498

[6] Maan B, van der Heijden F. Prostate MR image segmentation using 3d active appearance models. In: MICCAI 2012 Grand Challenge: Prostate MRI Image Segmentation; USA; 2012. pp. 44-51. doi: 10.1007/978-3-319-03731-8_20

[7] Korsager AS, Stephansen UL, Carl J, Ostergaard LR. The use of an active appearance model for automated prostate segmentation in magnetic resonance. Acta Oncologica 2013; 52 (7): 1374-1377. doi: 10.3109/0284186X.2013.822099

[8] Chandra SS, Dowling JA, Shen KK, Raniga P, Pluim JP et al. Patient specific prostate segmentation in 3-d magnetic resonance images. IEEE Transactions on Medical Imaging 2012; 31 (10): 1955-1964. doi: 10.1109/TMI.2012.2211377

[9] Vincent G, Guillard G, Bowes M. Fully automatic segmentation of the prostate using active appearance models. In: MICCAI 2012 Grand Challenge: Prostate MR Image Segmentation; USA; 2012. pp. 35-43. doi: 10.1371/journal.pone.0076645

[10] Ling M, Guo R, Tian Z, Venkataraman R, Sarkar S et al. A random walk-based segmentation framework for 3d ultrasound images of the prostate. Medical Physics 2017; 44 (10): 5128-5142. doi: 10.1002/mp.12396

[11] Egger J. Pcg-cut: graph driven segmentation of the prostate central gland. PLoS One 2013; 8 (10): e76645. doi: 10.1371/journal.pone.0076645

[12] Egger J, Mostarkic Z, Grosskopf S, Freisleben B. A fast vessel center line extraction algorithm for catheter simulation. In: CBMS 2007 Twentieth IEEE International Symposium on Computer Based Medical Systems; Maribor, Slovenia; 2007. pp.177-182. doi: 10.1109 /CBMS.2007.5

[13] Tian Z, Liu L, Zhang Z, Fei B. Superpixel-based segmentation for 3d prostate mr images. IEEE Transactions on Medical Imaging 2016; 35 (3): 791-801. doi: 10.1109/TMI.2015.2496296

[14] Mahapatra D. Graph cut based automatic prostate segmentation using learned semantic information. In: ISBI 2013 IEEE 10th International Symposium on Biomedical Imaging; San Francisco, CA, USA; 2013. pp. 1316-1319. doi: 10.1109/ISBI.2013.6556774

[15] Gao Y, Wang L, Shao Y, Shen D. Learning distance transform for boundary detection and deformable segmentation in ct prostate images. In: MLMI 2014 International Workshop on Machine Learning in Medical Imaging; Cham, Switzerland; 2014. pp. 93-100. doi: 10.1007/978-3-319-10581-9_12.

[16] Liao S, Gao Y, Shi Y, Yousuf A, Karademir I et al. Automatic prostate MR image segmentation with sparse label propagation and domain-specic manifold regularization. In: IPMI 2013 International Conference on Information Processing in Medical Imaging; Berlin, Germany; 2013. pp. 511-523. doi: 10.1007/978-3-642-38868-2_43

[17] Padgett K, Swallen A, Nelson A, Pollack A, Stoyanova R. Sufj171: Robust atlas based segmentation of the prostate and peripheral zone regions on mri utilizing multiple MRI system vendors. Medical Physics 2016; 43 (6): 3447-3447. doi: 10.1118/1.495607

[18] Khurd P, Grady L, Gajera K, Diallo M, Gall P et al. Facilitating 3d spectroscopic imaging through automatic prostate localization in MR images using random walker segmentation initialized via boosted classiers. In: International Workshop on Prostate Cancer Imaging; Berlin, Germany; 2011. pp. 47-56. doi: 10.1007/978-3-642-23944-1_5

[19] Ghose S, Mitra J, Oliver A, Marti R, Llado X et al. A supervised learning framework for automatic prostate segmentation in trans rectal ultrasound images. In: ACIVS 2012 International Conference on Advanced Concepts for Intelligent Vision Systems; Berlin, Germany; 2012. pp. 190-200. doi: 10.1007/ 978-3-642-33140-4_17

[20] Qiu W, Yuan J, Ukwatta E, Sun Y, Rajchl M et al. Fast globally optimal segmentation of 3d prostate MRI with axial symmetry prior. In: MICCAI 2013 International Conference on Medical Image Computing and Computer-Assisted Intervention; Berlin, Germany; 2013. pp. 198-205. doi: 10.1007/978-3-642-40763-5_25

[21] Yu L, Yang X, Chen H, Qin J, Heng PA. Volumetric convents with mixed residual connections for automated prostate segmentation from 3d MR images. In: AAAI 2017 Thirty-First Conference on Artificial Intelligence; San Francisco, CA, USA; 2017. pp. 66-72.

[22] Milletari F, Navab N, Ahmadi SA. V-net: Fully convolutional neural networks for volumetric medical image segmentation. In: 3DV 2016 Fourth International Conference on 3D Vision; Stanford, CA, USA; 2016. pp. 565-571. doi: 10.1109/3DV.2016.79

[23] He B, Xiao D, Hu Q, Jia F. Automatic magnetic resonance image prostate segmentation based on adaptive feature learning probability boosting tree initialization and CNN-ASM refinement. IEEE Access 2018; 6: 2005-2015. doi: 10.1109/ACCESS.2017.2781278

[24] Ling M, Guo R, Zhang G, Schuster DM, Fei B. A combined learning algorithm for prostate segmentation on 3d CT images. Medical Physics 2017; 44 (11): 5768-5781. doi: 10.1002/mp.12528

[25] Martin S, Troccaz J, Daanen V. Automated segmentation of the prostate in 3d MR images using a probabilistic atlas and a spatially constrained deformable model. Medical Physics 2010; 37 (4): 1579-1590. doi: 10.1118/1.3315367

[26] Drozdzal M, Chartrand G, Vorontsov E, Shakeri M, Di Jorio L et al. Learning normalized inputs for iterative estimation in medical image segmentation. Medical Image Analysis 2018; 44: 1-13. doi: 10.1016/j.media.2017.11.005

[27] Cootes TF, Edwards GJ, Taylor CJ. Active appearance models. IEEE Transactions on Pattern Analysis and Machine Intelligence 2001; 23: 681-685. doi: 10.1109/34.927467

[28] Bookstein FL. Principal warps: Thin-plate splines and the decomposition of deformations. IEEE Transactions on Pattern Analysis and Machine Intelligence 1989; 11 (6): 567-585. doi: 10.1109/34.24792.

[29] Awad J, Abdel-Galil T, Salama M, Tizhoosh H, Fenster A et al. Prostate's boundary detection in transrectal ultrasound images using scanning technique. In: IEEE CCECE 2003 Canadian Conference on Electrical and Computer Engineering; Montreal, Canada; 2003. pp. 1199-1202. doi: 10.1109/CCECE.2003.1226113

[30] Perona P, Malik J. Scale-space and edge detection using anisotropic diffusion. IEEE Transactions on Pattern Analysis and Machine Intelligence 1990; 12 (7): 629-639. doi: 10.1109/34.56205

[31] Xu C, Prince JL. Snakes, shapes, and gradient vector flow. IEEE Transactions on Image Processing 1998; 7 (3): 359-369. doi: 10.1109/83.661186

[32] Li B, Acton ST. Active contour external force using vector field convolution for image segmentation. IEEE Transactions on Image Processing 2007; 16 (8): 2096-2106. doi: 10.1109/TIP.2007.899601

[33] Salimi A, Pourmina A, Moien MS. Fully automatic prostate segmentation in MR images using a new hybrid active contour-based approach. Signal, Image and Video Processing 2018; 12 (8): 1629-1637. doi: 10.1007/s11760-018-1320-y